Title

Interfacial plasticity facilitates high reaction rate of E. coli FAS malonyl-CoA:ACP transacylase, FabD

Journal

Proceedings of the National Academy of Sciences of the United States of America, 117(39)

ISSN

0027-8424

Authors

Misson, Laetitia E
Mindrebo, Jeffrey T
Davis, Tony D
et al.

Publication Date

2020-09-29

DOI

10.1073/pnas.2009805117

Peer reviewed

Interfacial plasticity facilitates high reaction rate of *E. coli* FAS malonyl-CoA:ACP transacylase, FabD

Laetitia E. Misson[a,1], Jeffrey T. Mindrebo[a,b,1], Tony D. Davis[a,1], Ashay Patel[a,1], J. Andrew McCammon[a,c,2], Joseph P. Noel[b,2], and Michael D. Burkart[a,2]

[a]Department of Chemistry and Biochemistry, University of California San Diego, La Jolla, CA 92093-0358; [b]Jack H. Skirball Center for Chemical Biology and Proteomics, Salk Institute for Biological Studies, La Jolla, CA 92037; and [c]Department of Pharmacology, University of California San Diego, La Jolla, CA 92093-0358

Contributed by J. Andrew McCammon, July 14, 2020 (sent for review May 20, 2020; reviewed by Martin Grininger and Chung Wong)

Fatty acid synthases (FASs) and polyketide synthases (PKSs) iteratively elongate and often reduce two-carbon ketide units in de novo fatty acid and polyketide biosynthesis. Cycles of chain extensions in FAS and PKS are initiated by an acyltransferase (AT), which loads monomer units onto acyl carrier proteins (ACPs), small, flexible proteins that shuttle covalently linked intermediates between catalytic partners. Formation of productive ACP–AT interactions is required for catalysis and specificity within primary and secondary FAS and PKS pathways. Here, we use the *Escherichia coli* FAS AT, FabD, and its cognate ACP, AcpP, to interrogate type II FAS ACP–AT interactions. We utilize a covalent crosslinking probe to trap transient interactions between AcpP and FabD to elucidate the X-ray crystal structure of a type II ACP–AT complex. Our structural data are supported using a combination of mutational, crosslinking, and kinetic analyses, and long-timescale molecular dynamics (MD) simulations. Together, these complementary approaches reveal key catalytic features of FAS ACP–AT interactions. These mechanistic inferences suggest that AcpP adopts multiple, productive conformations at the AT binding interface, allowing the complex to sustain high transacylation rates. Furthermore, MD simulations support rigid body subdomain motions within the FabD structure that may play a key role in AT activity and substrate selectivity.

fatty acid biosynthesis | acyltransferase | acyl carrier protein | protein–protein interaction | plastic interface

Fatty acid synthases (FASs) and polyketide synthases (PKSs) iteratively condense and often reduce ketide units to assemble compounds ranging from simple fatty acids to complex bioactive molecules (1–4). FASs and PKSs exist as either multidomain megasynthases (type I) or as discrete monofunctional enzymes (type II). They both share a common evolutionary origin (3–7), and, therefore, FASs and PKSs often have related enzymatic components. Both systems require small, flexible acyl carrier proteins (ACPs) that are posttranslationally modified with phosphopantetheine (PPant) arms to shuttle covalently tethered reactive intermediates in the form of thioester bonds between catalytic partners. Catalysis is initiated by an acyltransferase (AT), which selects and loads starter and/or extender units onto the ACP. In type II FAS, extender units are loaded onto ACP via a malonyl-CoA:ACP transacylase (MAT), FabD, which catalyzes the transfer of the malonyl moiety from malonyl-CoA to the PPant arm of *holo*-ACP to form malonyl-ACP (Fig. 1). In contrast to type II FAS ATs, which only accept malonyl-CoA units, some ATs from PKSs accept a broader array of acyl-CoA units, as well as acyl-ACP units, increasing the structural diversity of their final products (1, 8–11). Interestingly, various bacterial type II PKS gene clusters lack a canonical AT to form malonyl-ACP. This activity is instead provided by the endogenous FAS MAT (12–14). The central catalytic role of PKS and FAS MATs makes them attractive candidates for metabolic engineering and as targets for the development of new therapeutics (15–20).

Engineering both type I and II FASs and PKSs is increasingly employed as a strategy to produce biofuels and bioactive natural products (8, 21–29). In this context, ATs are of particular interest as they act as gatekeepers that can direct the selection of key, biosynthetic building blocks. However, engineering efforts often lead to attenuated enzymatic activities (26, 30) or poorly soluble chimeras (31), likely due in part to an incomplete understanding of the transient nature of specific protein–protein interactions (PPIs) central to the iterative nature of FAS and PKS biosynthetic pathways. Interestingly, the high catalytic efficiency of FabD from *Escherichia coli*, which turns over substrate at nearly the diffusion limit (*SI Appendix*, Fig. S1) ($k_{cat}/K_M \sim 10^8\ s^{-1}{\cdot}M^{-1}$) (32, 33), makes this MAT a particularly attractive target to create a diverse collection of acyl-ACPs for type II FAS and PKS engineering (34, 35).

Descriptions of type II FAS and PKS ACP–MAT interfaces have benefited by docking simulations, NMR techniques, and binding affinity assays (14, 36, 37). While these studies suggest that MATs use shared binding motifs for malonyl-CoA and *holo*-ACP recognition, they often support different ACP–MAT binding interfaces. Recently, the X-ray crystal structures of two ACP–*trans*-AT

Significance

The essential role of acyltransferases (ATs) in fatty acid synthase (FAS) and polyketide synthase (PKS) pathways, namely the selection and loading of starter and extender units onto acyl carrier proteins (ACPs), relies on catalytically productive ACP–AT interactions. Here, we describe and interrogate the structure of a type II FAS malonyl-CoA:ACP-transacylase (MAT) in the covalent complex with its cognate ACP. We combine structural, mutational, crosslinking, and kinetic data with molecular dynamics simulations to describe a highly flexible and robust protein–protein interface, substrate-induced active site reorganization, and key subdomain motions that likely govern AT function. These findings strengthen a mechanistic understanding of molecular recognition between ACPs and partner enzymes and provide insights for engineering AT-dependent biosynthetic pathways.

Author contributions: L.E.M., J.T.M., T.D.D., A.P., J.A.M., J.P.N., and M.D.B. designed research; L.E.M., J.T.M., T.D.D., and A.P. performed research; J.A.M., J.P.N., and M.D.B. contributed new reagents/analytic tools; L.E.M., J.T.M., T.D.D., A.P., J.A.M., J.P.N., and M.D.B. analyzed data; and L.E.M., J.T.M., T.D.D., A.P., J.A.M., J.P.N., and M.D.B. wrote the paper.

Reviewers: M.G., Goethe University Frankfurt; and C.W., University of Missouri–St. Louis.

Competing interest statement: C.W. co-authored the preface of a 2016 special issue of the *Journal of Physical Chemistry B* that celebrates the life, career, and approach to science of J.A.M., who is a co-author of this work. For further information see the following: R.E. Amaro, J.D. Madura, C.F. Wong, Tribute to J. Andrew McCammon. *J Phys Chem B* 120(33):8055–8056 (2016).

[1]L.E.M., J.T.M., T.D.D., and A.P. contributed equally to this work.

[2]To whom correspondence may be addressed. Email: jmccammon@ucsd.edu, noel@salk.edu, or mburkart@ucsd.edu.

This article contains supporting information online at https://www.pnas.org/lookup/suppl/doi:10.1073/pnas.2009805117/-/DCSupplemental.

First published September 14, 2020.

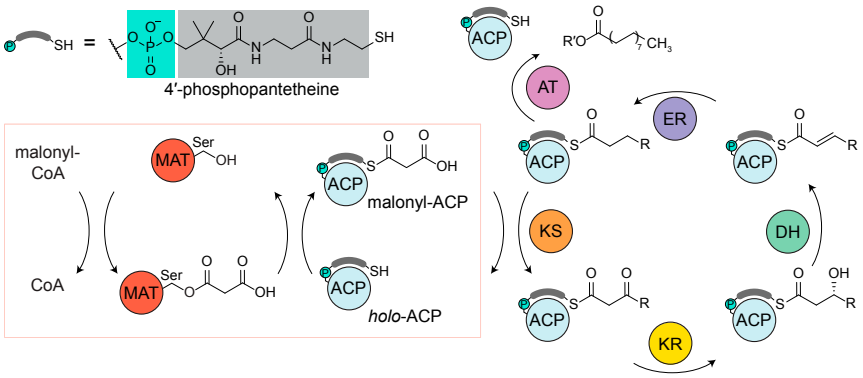

Fig. 1. Overview of saturated fatty acid biosynthesis from type II FAS, highlighting the function of malonyl-CoA:ACP transacylases (MATs). The MAT (dark orange) is transiently acylated at an active site serine residue by malonyl-CoA. Then, the malonyl group is transferred to the 4′-phosphopantetheine arm of *holo*-ACP (pale blue). Additional downstream FAS enzymes catalyze chain extension, modification, and release from the synthase: the ketoacyl-ACP synthases (KS, orange), the NAD(P)H-dependent ketoacyl-ACP reductase (KR, yellow), the dehydratases (DH, aqua marine), the NAD(P)H-dependent enoylreductase (ER, purple), and the glycerol-3-phosphate acyltransferases (AT, lavender). The R and R′ groups represent the omitted portion of the acyl-ACP thioester and the glycerol 3-phosphate–derived backbone of a phospholipid, respectively.

covalent complexes from the vicenistatin and disorazole type I PKS pathways were elucidated (38, 39). The ACP–AT binding modes and respective interface interactions in these structures present notable differences, and it remains unclear whether the molecular underpinnings of PKS ACP–*trans*-AT interactions are fully shared with type II ACP–MAT interactions.

To address this, we utilized active site-selective crosslinking to covalently capture *E. coli* FabD in association with its cognate ACP, AcpP, to facilitate the elucidation of the X-ray crystal structure of a type II FAS ACP–AT complex (PDB ID code 6U0J, 1.9 Å). We conducted biochemical assays that indicate the AcpP–FabD interface tolerates mutations to residues that initially appeared to support a specific and energetically stable protein–protein complex. In addition, we computationally probed this complex using long timescale molecular dynamics (MD) simulations. These computational studies support unanticipated plasticity at the AcpP–FabD interface, likely explaining FabD's tolerance to interface mutations with modest effects on turnover rates. A total of 32 μs of MD simulation data provides the most comprehensive sampling of AT dynamism to date, revealing rigid body subdomain motion, substrate-induced active site reorganization, and plasticity at the interface between the carrier protein and AT that likely explain the high catalytic rates of *E. coli* FabD. Our findings offer insights into the structures and dynamics of ACP–AT recognition in type II FASs. Collectively, these results open up additional possibilities and challenges directed toward the design of protein–protein interfaces that support AT-mediated catalysis for the engineering of novel metabolic outputs.

Results and Discussion

Crystallized Crosslinked Complex. In order to characterize the PPIs between a type II FAS ACP and its cognate AT, we crystallized a chemoenzymatically trapped complex of *E. coli* AcpP and its cognate AT, FabD. Classically, trapping covalent complexes between an ACP and a partner enzyme (PE) has been achieved through the synthesis of pantetheinamide crosslinking probes that react selectively and uniformly with the active site residues of the PE (40–42). These probes can be loaded onto an ACP via a one-pot chemoenzymatic method (43) to produce *crypto*-ACPs, which, when mixed with cognate PEs, form crosslinked complexes (44–47). Despite recent successes developing active site fluorescent probes for ATs (48), targeting the active site serine of FabD with complementary pantetheinamide probes proved challenging.

To produce sufficient quantities of crosslinked complexes for X-ray crystallography, we utilized a FabD S92C mutant that reacts with thiol-reactive pantetheinamide probes (39, 48, 49). Specifically, we generated C2-α-bromo-*crypto*-AcpP from *apo*-AcpP (*SI Appendix*, Fig. S2) (43), which was subsequently incubated with FabD S92C to produce a crosslinked AcpP–FabD complex (where the "–" denotes a covalent crosslink between the two proteins). This AcpP–FabD complex yielded diffraction quality crystals, resulting in the elucidation of a refined 1.9-Å-resolution structure (*SI Appendix*, Table S1). The complex crystallized in the C2 space group and the asymmetric unit contains one molecule of FabD crosslinked to a single AcpP.

Analysis of the 1.9-Å AcpP–FabD Structure. The refined structure displays exceptional electron density for FabD, AcpP, and the synthetic crosslinker (*SI Appendix*, Figs. S3 and S4). FabD comprises two subdomains, a larger α/β hydrolase (ABH) subdomain spanning residues 1 to 125 and 203 to 308, and a smaller ferredoxin-like (FL) subdomain spanning residues 126 to 202 (Fig. 2*A*). The active site of FabD is accessed along a large groove at the interface of the two subdomains, which also serves as the PPant/CoA binding site (Fig. 2*B*). AcpP is bound between the two FabD subdomains abutting the aforementioned groove. In total, the AcpP–FabD interface buries 350 $Å^2$ of surface area, making it the smallest reported AcpP–PE interface to date (42). The PPant arm extends from Ser36 of AcpP into the active site of FabD, where the α-carbon of the acetamide portion of the probe covalently attaches to the Cys92 mutant residue. The PPant arm makes a significant number of hydrophobic interactions derived almost exclusively from the FL subdomain of FabD, with the exception of Val280 from the ABH subdomain (Fig. 2*C*). Asn160, Asn162, and Gln166 line the floor of the groove, forming hydrogen bonding interactions with the PPant hydroxyl and amide functional groups (Fig. 2*C*). A sulfate ion from the crystallization buffer is bound in the active site and coordinates to the conserved Arg117 residue that forms a bidentate interaction with the terminal carboxylate of the malonyl substrate (*SI Appendix*, Figs. S1 and S5*A*) (50). The presence of the sulfate ion, the nonnative thioether crosslinked bond, and the C–S bond length cause the carbonyl group of the probe to rotate away from the oxyanion hole, which is formed by the backbone amides of Gln11 and Leu93, and instead accepts two hydrogen bonds from the N_δ of Asn160 and the N_ε of His202 (*SI Appendix*, Figs. S1 and S5*B*).

The FL and ABH subdomains in type I systems have been previously proposed to act as separate rigid bodies, with the FL subdomain capable of undergoing en bloc motions with respect to the larger ABH subdomain (51–53). These studies suggest FL subdomain mobility may be in part responsible for the reported

substrate promiscuity of the AT domain from murine FAS (51, 52). Given that FabD has undergone extensive structural characterization, we looked for potential changes in subdomain conformations induced by AcpP binding by performing a superposition using just the large ABH subdomains of *apo* FabD (PDB ID code 1MLA), malonyl-CoA-bound FabD (PDB ID code 2G2Z), and our AcpP–FabD crosslinked structure (PDB ID code 6U0J) (*SI Appendix*, Fig. S6). Indeed, these structural overlays show significant variations in the relative positioning of the two subdomains. The FL subdomain possesses a 5-Å, hinge-like displacement toward the ABH subdomain when comparing the *apo*-FabD and AcpP–FabD structures (*SI Appendix*, Fig. S6). The most notable structural changes induced by these subdomain motions are found in the loop exiting the β4 strand of the FL subdomain, referred to herein as the β4-loop. This loop translates to cover the top of the FabD active site and PPant binding tunnel and forms additional interactions between the two subdomains and the PPant moiety that are not present in either the *apo*-FabD (PDB ID code 1MLA) or the malonyl-CoA–bound FabD structures (PDB ID code 2G2Z) (*SI Appendix*, Fig. S7). Interestingly, the dihedral angles of residues in the β4-loop only differ at Ser197 and Val198 when comparing *apo*-FabD, malonyl-CoA–bound FabD, and AcpP–FabD, suggesting that movement of this loop is largely dictated by the FL subdomain rigid body motion.

The FL subdomain, including the β4-loop, in the malonyl-CoA–bound FabD structure (PDB ID code 2G2Z) exists in an intermediate conformation between the *apo*-FabD (PDB ID code 1MLA) and AcpP–FabD structures (PDB ID code 6U0J) (*SI Appendix*, Fig. S6). This is likely due to the positioning of the free thiol from the hydrolyzed CoA moiety present in the active site that would sterically clash with Leu194 and Val196 on the β4-loop (Fig. 2*D*). Despite these differences in conformation, the PPant arm of CoA and AcpP overlay almost identically in the two structures (Fig. 2*B*) and form a conserved hydrogen-bonding network with Asn160, Asn162, and Gln166 along the floor of the PPant binding tunnel (Fig. 2 *C* and *D*). It is worth noting that mutation of conserved residues along the β4-loop that precede the catalytic histidine (His-201 in FabD) results in changes in substrate

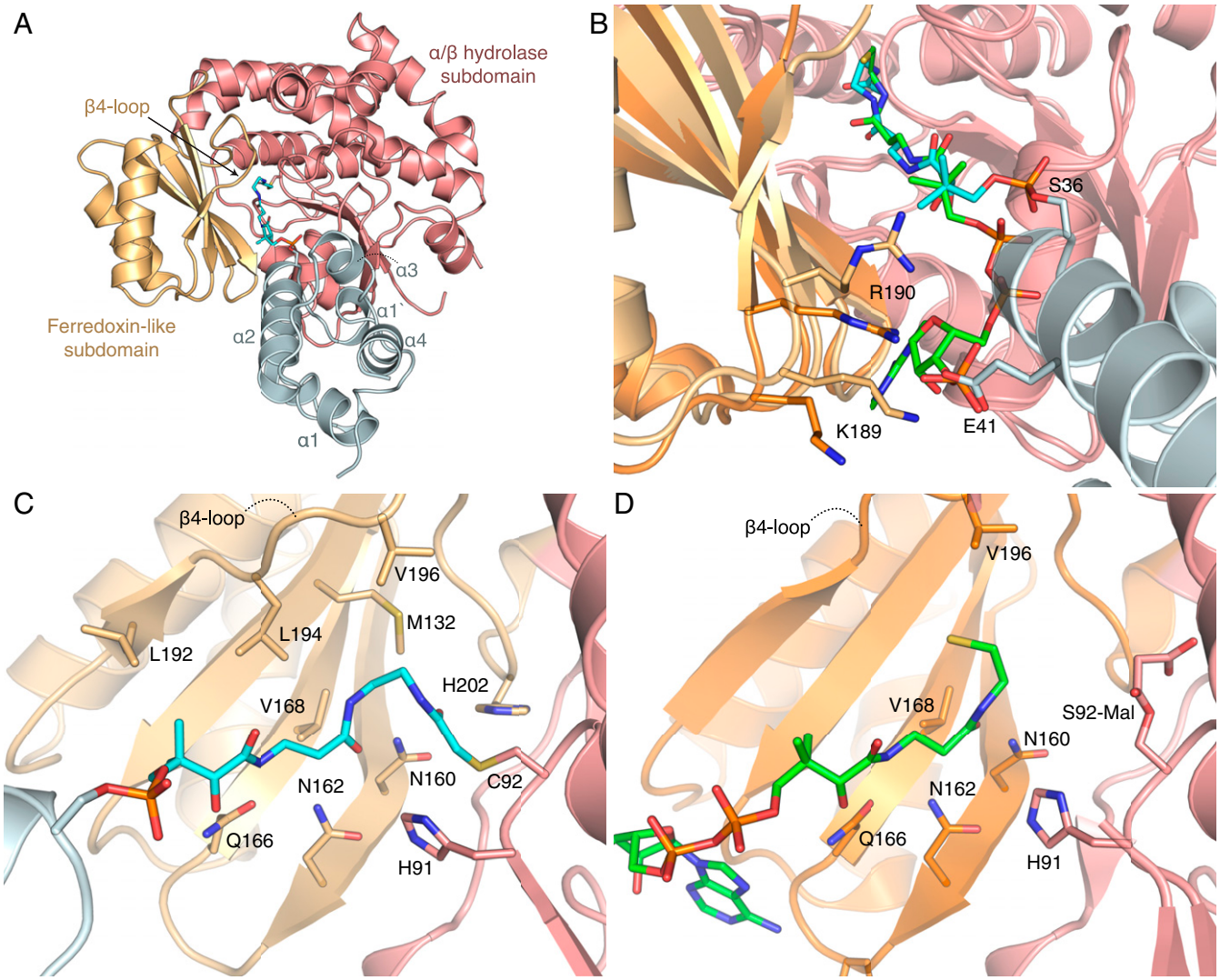

Fig. 2. AcpP–FabD crosslinked complex and PPant interactions. (*A*) Overall organization of the AcpP–FabD complex (PDB ID code 6U0J). (*B*) Overlay of malonyl-CoA-bound FabD (orange, PDB ID code 2G2Z) and AcpP–FabD (light orange, PDB ID code 6U0J) highlighting CoA/PPant binding groove and the similarities in interactions between CoA and *holo*-AcpP. The PPant arm (carbons colored cyan) and CoA (carbons colored green) are found in similar positions and conformations, and the 3′-phosphate of the CoA ribose ring is found in the same position as Glu41 of AcpP. (*C*) Interactions between the PPant arm (cyan) and FabD in AcpP–FabD structure (PDB ID code 6U0J). (*D*) Interactions between CoA (green) and FabD in malonyl-CoA–bound FabD structure (PDB ID code 2G2Z). A 4-Å distance cutoff was used to display FabD interacting residues in *C* and *D*. Only the interactions with the FL subdomain are shown for clarity in *C* and *D*.

specificities for type I PKS ATs. This may indicate that domain motions and the repositioning of the β4-loop over the active site play key roles in determining AT substrate selectivity and activity (11, 30, 54, 55).

Analysis of the AcpP–FabD Interface. Here, we describe the type II FAS ACP–AT complex from *E. coli*. Similar to all crosslinked AcpP–PE structures available (*SI Appendix*, Fig. S8) (44–47), electrostatic complementarity between AcpP and FabD facilitates molecular recognition, with the negatively charged AcpP interacting with a positive patch on FabD that likely drives initial association of AcpP and FabD (Fig. 3*A*). However, the AcpP–FabD crosslinked structure also departs from canonical FAS ACP binding motifs previously reported (42). It reveals a unique set of interfacial interactions between the two proteins involving the small helix on loop 1 of AcpP (α1′) and the N-terminal portion of helix II (α2) (Fig. 3 *B–D* and *SI Appendix*, Fig. S9). Additionally, unlike the dehydratases (FabA and FabZ) and elongating ketosynthases (FabB and FabF) in *E. coli* FAS, FabD makes no discernible contacts with helix III (α3) of AcpP (*SI Appendix*, Fig. S8). Notably, α3 interactions likely facilitate chain flipping (56) of AcpP-tethered cargo from the hydrophobic core of AcpP to the active sites of FabA, FabB, FabF, and FabZ (44, 46, 57). Since the PPant arm of FAS *holo*-ACPs does not sequester within the helical hydrophobic core (PDB ID codes 5H9H, 3GZM, 2M5R, and 2FQ0), the chain flipping process required for catalysis in these latter ACP–PE complexes is likely not operative in the delivery of the PPant arm of *holo*-ACP to the FabD active site (58–61). This may explain the lack of interfacial interactions involving α3 in the crosslinked AcpP–FabD structure.

The location of specific interactions of the AcpP–FabD interface can be delineated into three regions (Fig. 3 *B–D*). Region 1 comprises the C-terminal portion of the ABH subdomain, which forms interactions with α1′ of AcpP. Lys279 of FabD forms a salt bridge with Glu30 of AcpP, and Val29 of AcpP fits into a hydrophobic pocket created by Lys279, Thr282, and Gly283 of FabD (Fig. 3*B*).

Region 2 consists of Lys286 and Arg287, two conserved residues among bacterial type II MATs (*SI Appendix*, Fig. S10*A*). The key interactions in this region are between Arg287, modeled in two conformations, with both Asp35 and Asp38 at the top of AcpP's helix II flanking the PPant Ser36 (Fig. 3*C*). Interestingly, the guanidinium group of Arg287 forms cation-π stacking interactions with the adenine ring in the malonyl-CoA–bound FabD structure (PDB ID code 2G2Z), demonstrating its importance for both AcpP and malonyl-CoA binding (14, 36, 37, 50).

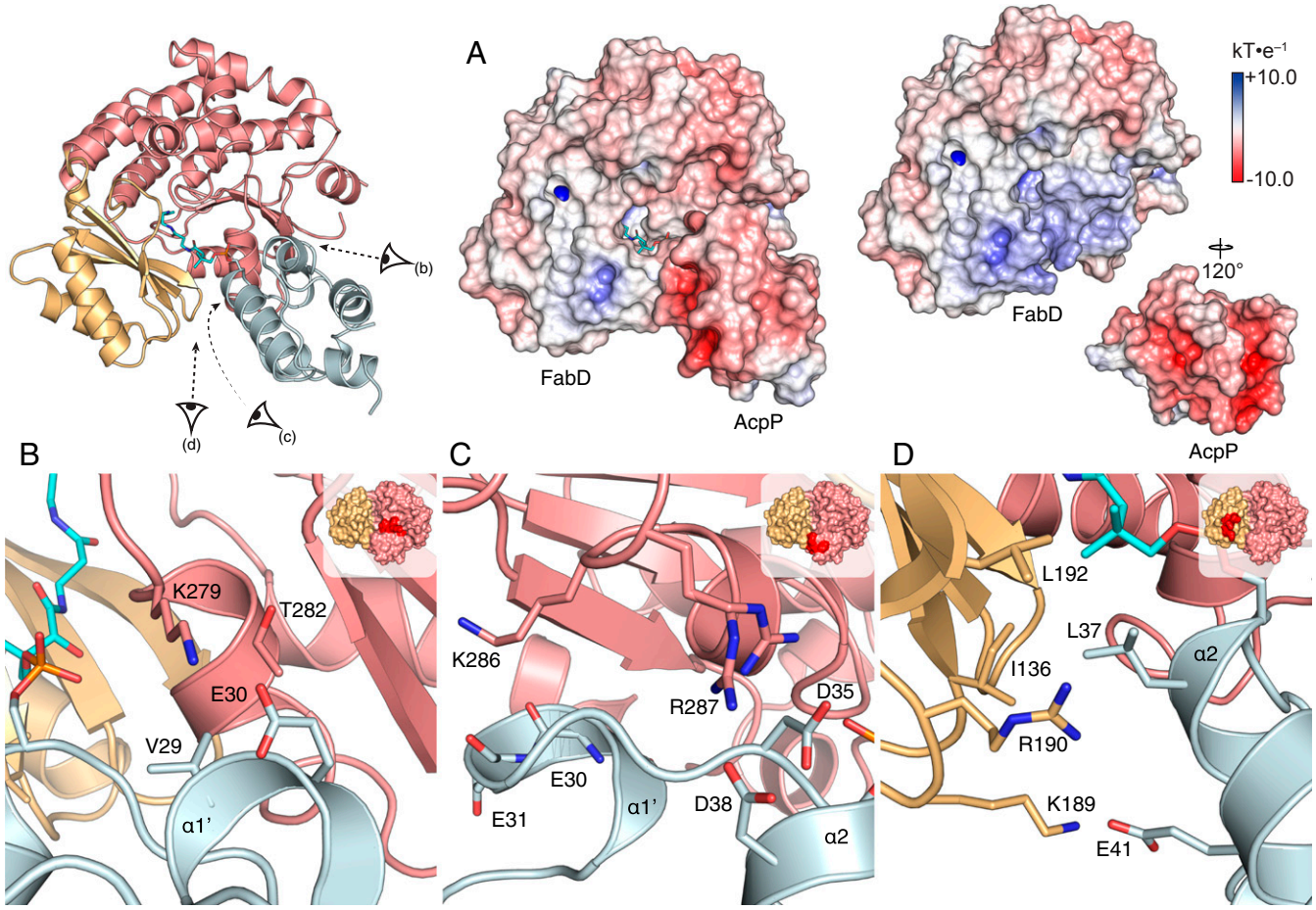

Fig. 3. AcpP–FabD interface. (*A*) AcpP–FabD, FabD, and AcpP electrostatic potentials (ESPs) mapped onto protein surface. In all cases, the ESPs are mapped onto the "Connelly" surfaces of the complex and monomers using a blue to white to red color range, spanning from +10.0 kT•e^{-1} to −10.0 kT•e^{-1}. (*B*) Region 1 of FabD–AcpP interface. (*C*) Region 2 of FabD–AcpP interface. Arg287 was modeled in two conformations, and both are shown. (*D*) Region 3 of FabD–AcpP interface. Arg190 delineates into two conformations, but only the conformation closest to AcpP is shown for clarity. A 4-Å distance cutoff was used to display AcpP–FabD-interacting residues in *B–D*, and the location of specific regions on FabD are shown as *Insets* in the top-right corner of each respective panel. Additionally, an overview of the AcpP–FabD complex showing perspective eyes for *B–D* is provided (*Top Left*). The ABH and FL subdomains of FabD, as well as AcpP, are shown in salmon, light orange, and light blue, respectively.

Region 3 is defined by the interactions between the FL subdomain and AcpP. In this region, Leu37 of AcpP sits in a hydrophobic groove formed by Ile136 and Leu192, and Glu41 from AcpP's α2 forms a salt bridge with Lys189 of FabD (Fig. 3*D*). Interestingly, overlays of AcpP–FabD and malonyl-CoA–bound FabD (PDB ID code 2G2Z) place the carboxylate side chain of Glu41 in the same location as the 3′-phosphate of the CoA ribose, indicating that CoA and AcpP form related interactions with FabD's interface region 3 (Fig. 2*B*). Despite the similarity in position, the CoA 3′-phosphate coordinates with Arg190 instead of Lys189, which is rotated away in the CoA-bound structure (Fig. 2*B*). Sequence alignments reveal that Lys189 is conserved among bacterial type II MATs whereas Arg190 is conserved among both bacterial type II and eukaryotic mitochondrial MATs (*SI Appendix*, Fig. S10*A*). It is worth noting that the electron density for the side chains of residues Glu41, Lys189, and Arg190 is not well-defined. Glu41 and Lys189 have high B-factors and Arg190 resides in two conformations, which suggests that the side chains of these residues are dynamic. In total, these data indicate that both Lys189 and Arg190 form interactions with Glu41 of AcpP.

In accordance with literature precedent (39, 47, 49, 62–65), we investigated PPIs for AcpP–FabD by comparing the crosslinking efficiencies of a panel of FabD S92C interface mutants with AcpP loaded with a C2-α-bromo-pantetheinamide probe (*SI Appendix*, Figs. S10 *B* and *C* and S11). Given that the FabD component of the interface is comprised almost exclusively of basic residues (Fig. 3 *B*–*D*), we generated three classes of FabD interface mutants: charge-neutralizing mutants (Arg to Ala or Lys to Ala), charge-conserving mutants (Arg to Lys), and charge-swapping mutants (Arg to Glu or Lys to Glu). The variants from the three regions have significantly reduced crosslinking efficiency compared to FabD S92C (*SI Appendix*, Fig. S10 *B* and *C*). The results from these crosslinking studies validate the structural conclusions and support the importance of the identified interface residues for complex formation.

Structural Comparison with *trans*-AT–ACP Interfaces. To date, only two other AT–ACP covalent complexes have been reported and analyzed, namely the *trans*-AT VinK in a covalent complex with VinL (38), and a second *trans*-AT from the disorazole synthase (DSZS) in a covalent complex with DSZS ACP1 (39). *Trans*-AT PKSs do not contain a *cis*-acting AT domain within their modules to deliver the extender units onto the ACP, but, instead, standalone ATs serve this role. VinK transfers a dipeptide intermediate between two ACPs (VinL and VinP1LdACP on the loading domain of module 1) during vicenistatin biosynthesis. DSZS is initiated by its *trans*-acting AT which malonylates the ACP of module 1. Elucidation of the AcpP–FabD complex allows analyses of the common features and differences of ACP recognition between modular type I *trans*-AT PKSs and type II FAS ATs. The overall subdomain organization of the three ATs, FabD, VinK, and DSZS AT (26.3% and 39.4% sequence identity with FabD, respectively) is similar, but the orientation of the ACPs notably differs between the three complexes. (Fig. 4 *A*–*C*). As observed in the AcpP–FabD complex, electrostatic contacts are important for both ACP–*trans*-AT complexes; however, hydrophobic interactions are more prominent features at the DSZS ACP1–DSZS AT and VinL–VinK interfaces than at the AcpP–FabD interface (Fig. 4 *D*–*F* and *SI Appendix*, Figs. S12 and S13) (38, 39). The differences observed between these structures calls for a deeper look into the structural elements of the AT enzyme class.

Effect of PPIs on FabD's Transacylation Reaction. We performed kinetic analyses of FabD mutants by using a continuous, coupled fluorometric assay in vitro (*SI Appendix*, Fig. S14) (66). We assayed our panel of FabD interface mutants along with three additional AcpP mutants: E30A, D38A, and E41A. These three AcpP residues participate in salt bridges across the interface of regions 1, 2, and 3, respectively (Fig. 3 *B*–*D*). All constructs were analyzed by sodium dodecyl sulfate polyacrylamide gel electrophoresis and mass spectrometry (*SI Appendix*, Fig. S15 and Table S2). The transacylation rates of the variants were measured at two concentrations of AcpP, 50 μM and 200 μM, which correspond to the concentrations of *holo*-AcpP at the K_M value and at saturation, respectively, for the wild-type (wt) system (*SI Appendix*, Fig. S16). The reaction rates were normalized to the transacylation rates of wt *holo*-AcpP by wt FabD

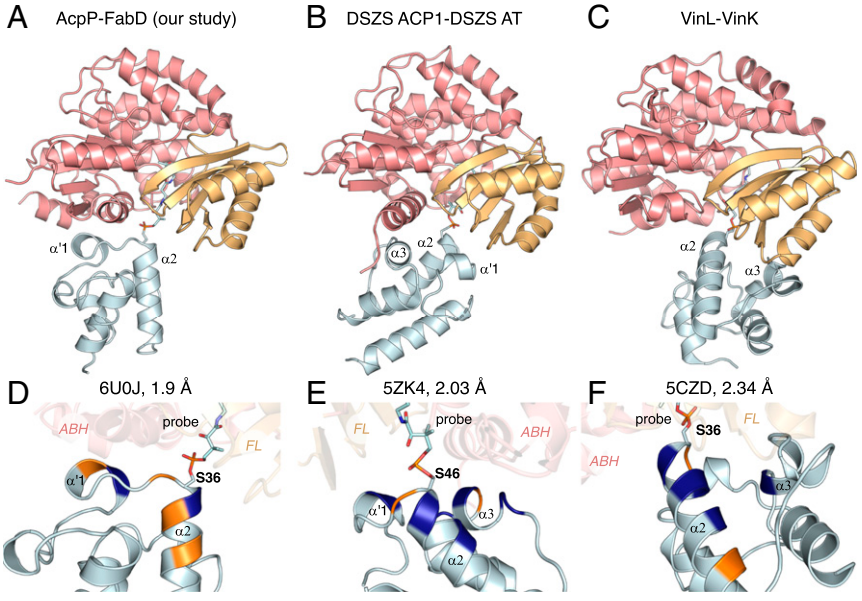

Fig. 4. Comparison of the AcpP–FabD complex with the ACP–*trans*-AT complexes DSZS ACP1-DSZS AT and VinL-VinK. (*A*–*C*) Schematic representation of the AcpP–FabD, DSZS ACP1–DSZS AT, and VinL–VinK complexes. The three complexes were aligned on FabD to better visualize the differences in ACP orientation. The FL and ABH subdomains of each AT are shown in light orange and salmon, respectively. The ACPs are colored in light blue. (*D*–*F*) Close-up views at the ACP–AT interface for the three complexes displaying the nature of the interactions: blue, hydrophobic; orange, electrophilic. The interacting helices, catalytic serine, and crosslinking probes are shown for each ACP. Note that *E* was rotated 180° from the above view to better visualize the interactions.

at the respective concentration of AcpP. This approach enables us to compare the effect of each interface mutant on FabD's activity (Table 1).

At $[ACP]_{200}$, only three FabD variants show a decrease in activity compared to wt: namely K189A, K279A, and K279E. At $[ACP]_{50}$, all tested FabD mutants have reduced activity compared to wt, except for region 2 variants R287K and R287A that remain as active as wt, and R287E shows a slight loss in activity. We hypothesized that, upon mutation of Arg287 to alanine, the fairly conserved Lys286 (*SI Appendix*, Fig. S10*A*) might have the rotational freedom to interact with Asp38 and compensate for the loss of the salt bridge between Arg287 and Asp38. We therefore tested the double mutant K286A/R287A, which remains as active as wt FabD for both AcpP concentrations. On the contrary, mutation of Lys279 in region 1 to either alanine or glutamate results in a larger decrease in relative activity as compared to FabD region 2 variants. Similarly, mutating Lys189 from region 3 also more significantly affects FabD activity, with a greater effect seen with the charge-swapped mutant K189E, as compared to the charge-neutralized variant K189A. To determine whether Arg190 participates in AcpP recognition despite its lack of discernible interactions in our AcpP–FabD structure, we evaluated the catalytic activity of R190A and K189A/R190A mutants. The R190A variant is similar in activity to wt while the double mutant K189A/R190A is less active than K189A but faster than K189E. These data suggest that the interactions with the FL subdomain are mediated by both Lys189 and Arg190.

In addition to kinetically evaluating FabD interface residues, we also analyzed the transacylation rates of AcpP interface mutants E30A, D38A, and E41A that coordinate interactions with FabD regions 1, 2, and 3, respectively. Interestingly, these mutations are less detrimental to FabD transacylation rates than their corresponding FabD interface mutants. In order to determine if the AcpP and FabD interface mutations were additive, we eliminated the three salt bridges at the interface by testing FabD interface mutants with their respective AcpP mutant counterparts. While assays of AcpP D38A and region 2 FabD mutants result in no more than a 50% drop in activity for all combinations tested, significantly slower transacylation rates were observed by combining mutant pairs from regions 1 and 3.

Results from all tested FabD and AcpP mutants demonstrate that the AcpP–FabD interface can tolerate mutations of residues that appear to be critical from the static crystal structure. We find that mutations on the FabD interface are more detrimental than their corresponding AcpP mutants, which may be due to the dynamic nature of AcpP. Our activity assays also show that mutating key residues on regions 1 and 3 of the FabD interface seems to influence the transacylation reaction more than region 2. Nevertheless, most mutations, even double mutants assayed with their corresponding AcpP mutant counterparts, do not abolish FabD's activity.

Dynamic Analysis of the AcpP–FabD Interface. The tolerance of the FabD interface to mutations, as indicated by our kinetic analyses, suggests flexible interactions between AcpP and FabD. Therefore, to further our understanding of the biomolecular processes that contribute to AcpP–FabD recognition, we subjected 17 protein assemblies, consisting of wt FabD and FabD mutants in the

Table 1. Quantification of the transacylation rates of AcpP–FabD interface mutants

FabD	AcpP	Relative activity at $[ACP]_{50}$, %	Relative activity at $[ACP]_{200}$, %
Wild type	Wild type	100.0	100.0
K279A	Wild type	30.3 ± 6.9	23.9 ± 3.5
K279E	Wild type	30.6 ± 7.6	30.2 ± 5.2
Wild type	E30A	85.1 ± 7.9	99.5 ± 11.1
K279A	E30A	84.7 ± 10.3	n.a.
K279E	E30A	14.2 ± 7.5	n.a.
R287K	Wild type	93.6 ± 3.2	102.7 ± 8.5
R287A	Wild type	92.7 ± 9.4	89.0 ± 12.9
R287E	Wild type	81.1 ± 7.8	99.6 ± 6.2
Wild type	D38A	69.5 ± 4.8	83.2 ± 9.3
R287K	D38A	55.7 ± 5.4	n.a.
R287A	D38A	77.3 ± 3.2	n.a.
R287E	D38A	53.1 ± 6.9	n.a.
K286A	Wild type	63.1 ± 10.3	99.0 ± 10.5
K286A/R287A	Wild type	96.8 ± 13.7	104.9 ± 13.9
K286A/R287A	D38A	77.9 ± 1.1	n.a.
K189A	Wild type	67.9 ± 7.3	77.4 ± 17.3
K189E	Wild type	26.2 ± 4.8	104.0 ± 2
Wild type	E41A	90.1 ± 1.9	95.8 ± 4.1
K189A	E41A	30.6 ± 2.1	n.a.
K189E	E41A	10.6 ± 3.0	n.a.
R190A	Wild type	103.5 ± 9.5	n.a.
K189A/R190A	Wild type	40.1 ± 4.7	114.1 ± 8.7
K189A/R190A	E41A	15.2 ± 1.8	n.a.
L192A	Wild type	67.5 ± 8.2	101.0 ± 13.4

Reaction conditions were as follows: 28 °C, 50 mM sodium phosphate, pH 6.8, 1 mM (Ethylenediamine)tetraacetic acid, 0.5 mM Tris(2-carboxyethyl)phosphine, 2 mM α-ketoglutarate, 0.4 mM NAD^+, 0.4 mM thiamine pyrophosphate, 15 mU/100 μL α-ketoglutarate dehydrogenase, and 0.02 nM FabD. $[ACP]_{50}$ corresponds to 50 μM *holo*-AcpP and 50 μM malonyl-CoA; $[ACP]_{200}$ corresponds to 200 μM *holo*-AcpP and 200 μM malonyl-CoA. The activity of each interface mutant was measured at the fixed concentration of AcpP indicated and was normalized to the corresponding activity of wt FabD, with wt AcpP for each tested condition (*SI Appendix, Relative activities of FabD and AcpP mutants*). Experiments were run at least in triplicate, and data shown are reported as mean ± SD. Table entries containing the term "n.a." (not applicable) indicate AcpP•FabD systems for which no data is available.

apo-, malonyl-CoA–, and malonyl-AcpP–bound states (*SI Appendix*, Table S3), to MD simulations. We performed three independent 514-ns production-grade trajectories for each wt and mutant system, resulting in a total of 32.382 μs of simulation data. General analysis of these trajectories can be found in *SI Appendix*, *Molecular Dynamics Simulations Protocols*, as well as in *SI Appendix*, Figs. S17–S24.

We analyzed trajectory data of the wt and mutant malonyl-AcpP•FabD complexes (where the "•" denotes a noncovalent complex) in order to propose a time-resolved understanding of the noncovalent interactions most critical for AcpP•FabD recognition. To do so, we identified all pairwise AcpP and FabD interactions that form over the course of the simulations using a 3.5-Å distance cutoff criterion (Fig. 5). This analysis generally shows that the interactions at the AcpP•FabD interface are dynamic, and a number of interactions not observed in the X-ray structure are identified during the course of the simulations. Interestingly, none of the hydrophobic interactions identified in the AcpP–FabD structure were observed computationally (Fig. 5). In contrast, the salt bridges identified in the X-ray structure are observed over the course of the simulations; however, they are in rapid exchange with an alternate set of salt bridges that are not resolved experimentally (Fig. 5*B*). For example, the most frequently sampled salt bridge interaction between AcpP and FabD is a contact between Glu41 and Arg190 not present in the X-ray structure. Simulations of the malonyl-AcpP•FabD mutant complexes show the same general trend as the wt system and indicate that there are compensatory interactions that can be formed to stabilize these complexes despite the removal of key interface residues (Fig. 5).

Given the rotational and translational motion of AcpP at the interface, we reasoned that these conformational changes may affect substrate organization in the FabD binding pocket. Interestingly, the contact between the malonyl carboxylate of malonyl-AcpP and the FabD active site Arg117, as well as the Ser92-His201 catalytic dyad distance, are maintained throughout the simulations despite the positional variation of AcpP (*SI Appendix*, Figs. S25 and S26). Taken together, these data suggest significant plasticity in the AcpP•FabD interface and provide a rationale for FabD's tolerance to interface mutations as AcpP can adopt multiple conformations at the FabD interface, while still properly positioning substrate in the active site for catalysis. In addition, our findings corroborate the smaller reduction of transacylation activity for AcpP mutations as compared to corresponding FabD mutations as AcpP can rotate at the interface to form compensatory interactions (Fig. 5).

Substrate-Induced Reorganization of the FabD Active Site. To determine the effect of substrate binding on active site organization, we performed a time-resolved analysis of interactions involving the conserved active site residues Ser92, Arg117, and His201. The positively charged Arg117 residue has been shown to influence the preferences of ATs for α-carboxy-CoA substrates over α-descarboxy analogs. For example, the R117A mutant of FabD loads a number of α-descarboxy-CoA derivatives, including acetyl-CoA (35). Furthermore, Rangan and Smith show that a

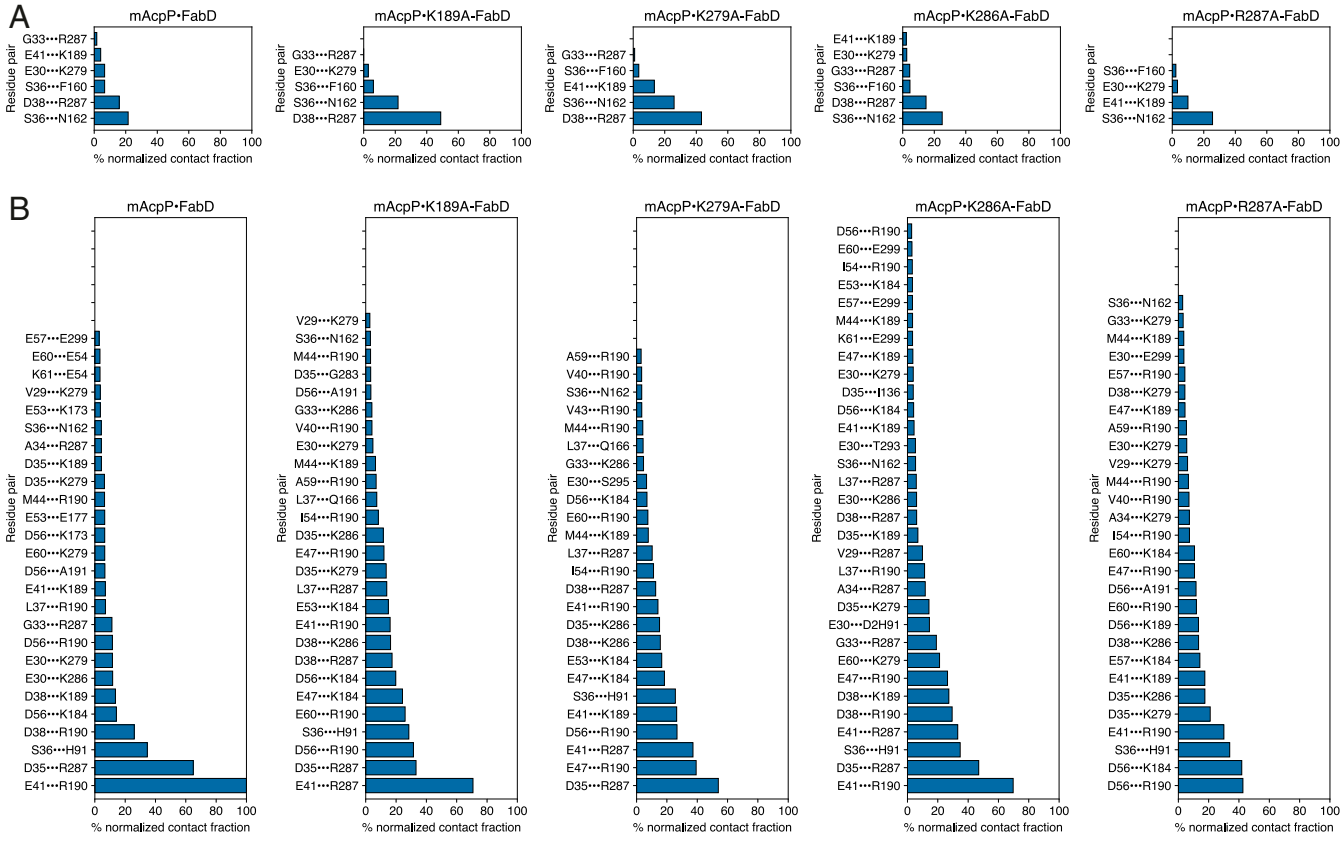

Fig. 5. Time-resolved analysis of the contacts formed between FabD (wt and four variants) and its binding partner malonyl-AcpP (mAcpP). Contacts from the initial conditions and contacts formed during the course of the simulations are shown in *A* and *B*, respectively. The analyzed FabD (wt, K189A, K279A, K286A, or R287A) is indicated on the top of each bar graph. Residues listed on the left side of the interaction pair correspond to AcpP, and those on the right side of the pair correspond to FabD. The bar graphs indicate the normalized total contact fraction between FabD and malonyl-AcpP. The contact fraction is defined as the total fraction of simulation data in which a residue pair is engaged in an intermolecular contact. A distance criterion of 3.5 Å or less between a pair of heavy atoms defines such a contact. Only pairwise contacts with contact fractions (prior to normalization) greater than or equal to 0.10 are included in the bar graphs shown above.

similar Arg-to-Ala mutant of the malonyl-CoA/acetyl-CoA:ACP transferase of animal FAS results in a 100-fold decrease in its malonyl-CoA transferase activity, while its acetyl-CoA transferase activity is enhanced 6.6-fold (67). Studies by Dunn et al. indicate that substrate discrimination occurs before the CoA substrate undergoes reaction at the AT active site and not by preferential hydrolysis of "misacylated" ATs after transacylation (30).

MD simulations of *apo*-FabD suggest a possible mechanistic explanation for the broad role of Arg117 in regulating substrate selectivity in MATs. Analysis of simulation data of *apo*-FabD shows that, in the absence of a substrate, the average distance between the Oγ of Ser92 and the center of geometry (COG) of Arg117's terminal guanidinium moiety is 3.68 Å (Fig. 6*A*). It must be noted that measuring from the arginine, histidine, or carboxylate COG reports distances larger than are typical of noncovalent interactions (68). Thus, simulation data show that the dyad residues, Ser92 and His201, are not preorganized for catalysis in the *apo* state because Ser92 interacts stably with Arg117 (Fig. 6*A*). Interestingly, simulations of *E. coli* malonyl-CoA•FabD show that α-carboxy-CoA substrate binding disrupts the Ser92–Arg117 interaction, which in turn restores the Ser–His dyad (*SI Appendix*, Figs. S25–S29). The average distances between the COG of Arg117 and the COG of malonyl carboxylate are 2.73 Å and 2.79 Å in simulations of wt malonyl-CoA•FabD (*SI Appendix*, Fig. S24) and wt malonyl-AcpP•FabD (*SI Appendix*, Fig. S29), respectively, suggesting a strong salt bridge interaction between substrate and enzyme in the bound state. With Arg117 engaged with the substrate, the catalytic dyad is restored as the average distance between the Oγ of Ser92 and His201's $N_{\varepsilon}2$ sampled computationally is 3.40 Å and 2.95 Å for malonyl-AcpP•FabD and malonyl-CoA•FabD, respectively, more than 1 Å shorter than what is observed over the course of simulations of *apo*-FabD (Fig. 6 *A*–*C*). These results suggest that substrate binding organizes the FabD active site for catalysis and provides an explanation for FabD's (and MATs more broadly) preference for malonyl-CoAs or malonyl-AcpP over acetyl-CoA (35).

Rigid Body Subdomain Motions Control the Disposition of Substrate-Recognizing Residues. Recent studies on the murine FAS AT have suggested that rigid body FL and ABH subdomain motion may play a role in determining AT substrate selectivity (51, 52). Superpositions of our AcpP–FabD complex with the *apo*- and malonyl-CoA–bound FabD structures provide additional evidence for the occurrence of such motions (*SI Appendix*, Fig. S6). Moreover, biochemical and structural data implicate residues found on the β4-loop of the FL subdomain, in particular those that immediately precede the catalytic histidine of ATs (His201 in FabD), play a role in determining AT preferences for α-branched vs. nonbranched α-carboxy-CoA substrates (11, 30, 54, 55). These residues (Val198, Ser199, and Phe200 in FabD) define part of the enzyme's active site pocket, and their steric bulk permits or prevents the binding of α-branched CoA substrates. We reason that rigid body motion of the FL subdomain, if present, may play a role in organizing the active site to preferentially accept either branched or nonbranched CoA substrates. Therefore, we performed principal component analysis (PCA) to identify and highlight large-scale motions of the FL and ABH subdomains that may impact the activity and

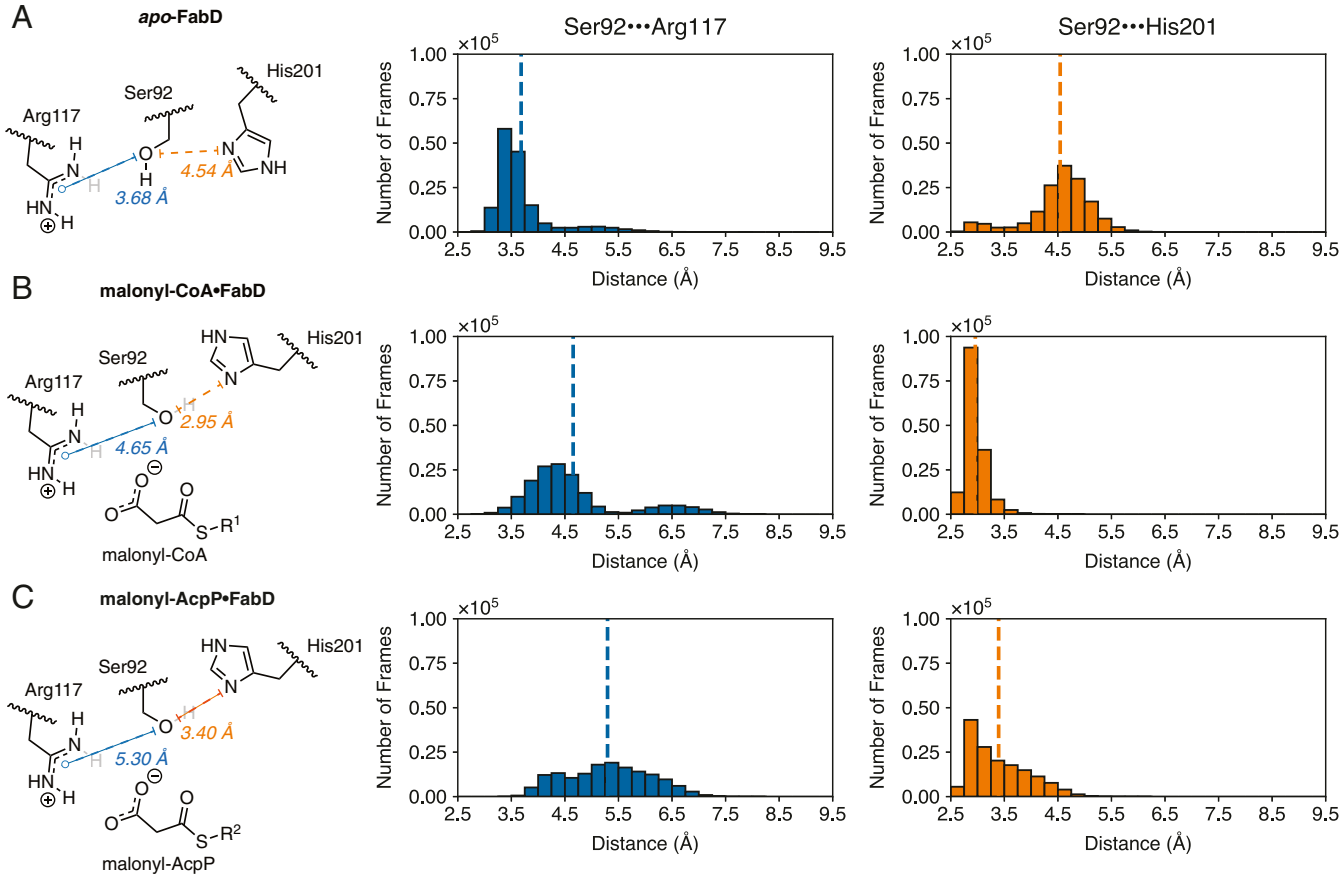

Fig. 6. Analysis of key active site distances sampled in the *apo*- and substrate-bound states of FabD. Distribution of distances between two pairs of active site residues Ser92•••His201 and Ser92•••Arg117 sampled over the course of simulations of wt *apo*-FabD (*A*), malonyl-CoA•FabD (*B*), and malonyl-AcpP•FabD (*C*). The distance between Ser92 and His201 is measured using the Oγ of Ser92 and Nε of His-201 while the Ser92•••Arg117 distance is measured using the Oγ of Ser92 and the COG of Arg117's guanidium moiety. Simulation data written every 0.5 ps were binned to prepare histograms using a bin width of 0.25 Å.

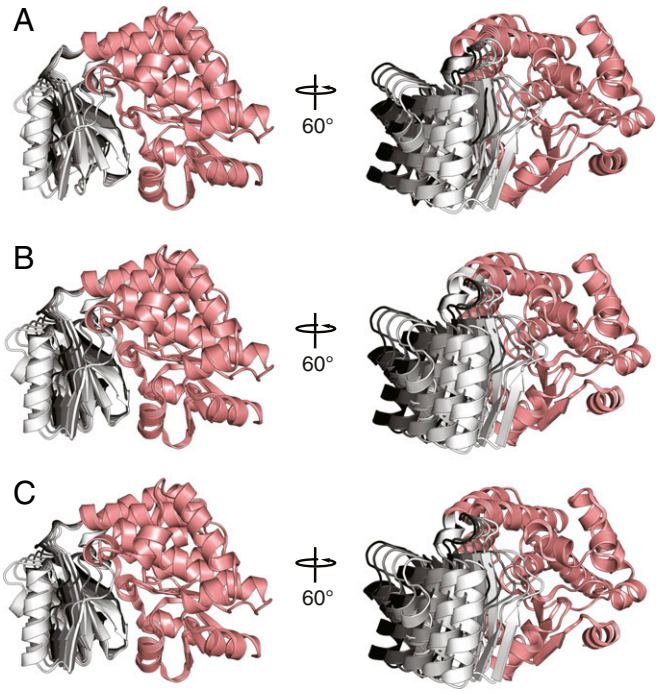

Fig. 7. Projection of principal component analysis data into coordinate space. Overlaid snapshots of the pseudotrajectories illustrating the first mode of motion of the FabD monomer portions of (*A*) *apo*-FabD, (*B*) malonyl-CoA•FabD, and (*C*) malonyl-AcpP•FabD. The ABH subdomains are colored salmon while the FL subdomains are colored based upon the distance between the FL subdomain, such that more darkly colored subdomains are further from the ABH subdomain.

substrate specificity of FabD. Our analysis incorporates coordinate data from wt and mutants of *apo*-FabD (10.794 μs of simulation data), malonyl-CoA•FabD (9.252 μs of simulation data), and malonyl-AcpP•FabD (9.252 μs of simulation data).

Projections of the first principal component (determined via PCA) onto our coordinate data support the hypothesis that the FL and ABH subdomains act as rigid bodies involving the displacement and rotation of the smaller FL subdomain away from ABH subdomain (Fig. 7). That this motion is represented by the first principal component, the orthogonal component with the largest variance (i.e., most dominant "mode" describing FabD motion), supports its role as an essential feature of FabD's function. A comparison of the first principal components generated from the dataset described above indicates that, as suggested by the comparison of X-ray structures presented in *SI Appendix*, Fig. S6, the FL subdomain moves independently of the ABH subdomain (Fig. 7 and Movies S1–S3). The rigid body motions evaluated computationally disambiguate a motion of FL subdomain toward and away from the ABH domain to gate substrate access to and from the active site. In addition to active site gating, this rigid body motion also results in the movement of the β4-loop toward the base of the active site, not only organizing the His201 for catalysis, but also positioning the key substrate-sensing residues Val198, Ser199, and Phe200 to selectively interact with *E. coli* FabD's preferred substrate (Movies S1–S3).

Conclusion

In this study, we used *E. coli* type II FAS as a structural and mechanistic model to better understand type II ACP–AT interactions and their catalytic role in fatty acid biosynthesis. Utilizing a pantetheinamide covalent crosslinking probe, we trapped and crystallized the *E. coli* ACP, AcpP, in complex with FabD, allowing us to elucidate the crystal structure of a type II ACP–AT complex at 1.9 Å resolution. The AcpP–FabD binding mode is different from previously described AcpP complexes and represents the smallest AcpP–PE interface reported to date. Despite the small number of experimentally determined interfacial interactions, mutation of these interface residues does not result in significant reductions in FabD transacylation activity. Long timescale MD simulations of AcpP in complex with wt FabD and FabD interface mutants demonstrate that AcpP can undergo considerable rotational and translational motion at the FabD interface, while still properly positioning its PPant-tethered substrate for catalysis. These results are in line with kinetic analyses of FabD interface mutants and suggest a high-plasticity interface dominated by polar and charged interactions that are in rapid exchange. Furthermore, MD analysis of FabD in both its liganded and unliganded states corroborate the presence of en bloc rigid body motions of its FL and ABH subdomains and provide additional insights into Arg117's role in substrate-mediated reorganization of the FabD active site. Taken together, these findings represent a significant advancement in our understanding of type II ACP–AT interactions, AT dynamics, and AT substrate selectivity. The structural, biochemical, and computational analyses of these systems reported herein represent another necessary step toward a broader and more complete understanding of PPIs in type II FAS and natural product biosynthesis.

Materials and Methods

Experimental Methods. The methods for FabD and AcpP protein expression and purification are described in *SI Appendix*. The crosslinked FabD–AcpP complex was crystallized by vapor-diffusion using the hanging drop method. All X-ray datasets were collected at the Advanced Light Source (ALS) synchrotron at the Lawrence Berkeley National Laboratory. Information regarding X-ray data indexing, processing, and model building can be found in *SI Appendix, SI Materials and Methods*. The FabD and AcpP mutants were prepared by site-directed mutagenesis. Kinetic analyses of FabD were performed by using a continuous, coupled fluorometric assay in vitro. Full details for all experimental protocols are described in *SI Appendix, SI Materials and Methods*.

Computational Methods. For simulation work, the coordinates of the wild-type and mutant *apo*-FabD, malonyl-CoA•FabD, and malonyl-AcpP•FabD structures were generated using X-ray crystal structures of *apo*-FabD (PDB ID codes 1MLA and 2G1H) malonyl-CoA-bound FabD (PDB ID code 2G2Z), and the crosslinked AcpP–FabD (reported herein), respectively. Simulations were performed using graphics processing unit (GPU)-accelerated Amber 2016 and Amber 2018. Full details for all computational protocols are described in *SI Appendix, SI Materials and Methods*.

Data Availability. The atomic coordinates and structure factors have been deposited in the Protein Data Bank (PDB ID code 6U0J). All other study data are included in the article and *SI Appendix*.

ACKNOWLEDGMENTS. This work was supported by NIH Grants GM095970 (to M.D.B.) and GM31749 (to J.A.M). L.E.M. was supported by an Early Postdoctoral Mobility Fellowship from the Swiss National Science Foundation. J.T.M. was supported by Molecular Biophysics Training Grant, NIH T32 GM008326. T.D.D. is a San Diego Institutional Research and Academic Career Development Award Postdoctoral Fellow supported by NIH Grants K12 GM068524 and K99 GM129454. Portions of the work were also funded by the Arthur and Julie Woodrow Chair at the Salk Institute (J.P.N.) and the HHMI (J.P.N.). We thank Dr. Gordon Louie for assistance in X-ray data collection, processing, and refinement; Marianne Bowman for assistance with protein crystallization; the University of California San Diego Chemistry and Biochemistry Mass Spectrometry Facility for the molecular weight determination of FabD and AcpP wt and variants used in the kinetic assays; and Dr. Anthony Mrse for NMR assistance. We thank the San Diego Supercomputer Center for the provision of the computational resources used to perform computer simulations described herein.

1. C. Hertweck, The biosynthetic logic of polyketide diversity. *Angew. Chem. Int. Ed. Engl.* **48**, 4688–4716 (2009).
2. T. Maier, M. Leibundgut, D. Boehringer, N. Ban, Structure and function of eukaryotic fatty acid synthases. *Q. Rev. Biophys.* **43**, 373–422 (2010).
3. D. A. Herbst, C. A. Townsend, T. Maier, The architectures of iterative type I PKS and FAS. *Nat. Prod. Rep.* **35**, 1046–1069 (2018).
4. J. E. Cronan, J. Thomas, Bacterial fatty acid synthesis and its relationships with polyketide synthetic pathways. *Methods Enzymol.* **459**, 395–433 (2009).

5. G. S. Kohli, U. John, F. M. Van Dolah, S. A. Murray, Evolutionary distinctiveness of fatty acid and polyketide synthesis in eukaryotes. *ISME J.* **10**, 1877–1890 (2016).
6. M. E. Hillenmeyer, G. A. Vandova, E. E. Berlew, L. K. Charkoudian, Evolution of chemical diversity by coordinated gene swaps in type II polyketide gene clusters. *Proc. Natl. Acad. Sci. U.S.A.* **112**, 13952–13957 (2015).
7. M. Grininger, Perspectives on the evolution, assembly and conformational dynamics of fatty acid synthase type I (FAS I) systems. *Curr. Opin. Struct. Biol.* **25**, 49–56 (2014).
8. L. Ray, B. S. Moore, Recent advances in the biosynthesis of unusual polyketide synthase substrates. *Nat. Prod. Rep.* **33**, 150–161 (2016).
9. B. J. Dunn, C. Khosla, Engineering the acyltransferase substrate specificity of assembly line polyketide synthases. *J. R. Soc. Interface* **10**, 20130297 (2013).
10. J. M. Winter *et al*., Biochemical and structural basis for controlling chemical modularity in fungal polyketide biosynthesis. *J. Am. Chem. Soc.* **137**, 9885–9893 (2015).
11. H. Park, B. M. Kevany, D. H. Dyer, M. G. Thomas, K. T. Forest, A polyketide synthase acyltransferase domain structure suggests a recognition mechanism for its hydroxymalonyl-acyl carrier protein substrate. *PLoS One* **9**, e110965 (2014).
12. F. Ishikawa, H. Sugimoto, H. Kakeya, In vitro investigation of crosstalk between fatty acid and polyketide synthases in the andrimid biosynthetic assembly line. *ChemBioChem* **17**, 2137–2142 (2016).
13. B. J. Rawlings, Biosynthesis of polyketides (other than actinomycete macrolides). *Nat. Prod. Rep.* **16**, 425–484 (1999).
14. C. J. Arthur *et al*., Structure and malonyl CoA-ACP transacylase binding of *streptomyces coelicolor* fatty acid synthase acyl carrier protein. *ACS Chem. Biol.* **4**, 625–636 (2009).
15. W. Liu *et al*., Characterization and inhibitor discovery of one novel malonyl-CoA: Acyl carrier protein transacylase (MCAT) from *Helicobacter pylori*. *FEBS Lett.* **580**, 697–702 (2006).
16. V. Kumar, A. Sharma, S. Pratap, P. Kumar, Biochemical and biophysical characterization of 1,4-naphthoquinone as a dual inhibitor of two key enzymes of type II fatty acid biosynthesis from *Moraxella catarrhalis*. *Biochim. Biophys. Acta. Proteins Proteomics* **1866**, 1131–1142 (2018).
17. W. C. Lee, J. Park, P. K. Balasubramanian, Y. Kim, Elucidation of the crystal structure of FabD from the multidrug-resistant bacterium *Acinetobacter baumannii*. *Biochem. Biophys. Res. Commun.* **505**, 208–214 (2018).
18. V. Kumar, A. Sharma, S. Pratap, P. Kumar, Biophysical and in silico interaction studies of aporphine alkaloids with Malonyl-CoA: ACP transacylase (FabD) from drug resistant *Moraxella catarrhalis*. *Biochimie* **149**, 18–33 (2018).
19. X. Zhang, A. Agrawal, K. Y. San, Improving fatty acid production in *Escherichia coli* through the overexpression of malonyl coA-acyl carrier protein transacylase. *Biotechnol. Prog.* **28**, 60–65 (2012).
20. H. Ghadbane, A. K. Brown, L. Kremer, G. S. Besra, K. Fütterer, Structure of *Mycobacterium tuberculosis* mtFabD, a malonyl-CoA:acyl carrier protein transacylase (MCAT). *Acta Crystallogr. Sect. F Struct. Biol. Cryst. Commun.* **63**, 831–835 (2007).
21. J. Gajewski, R. Pavlovic, M. Fischer, E. Boles, M. Grininger, Engineering fungal *de novo* fatty acid synthesis for short chain fatty acid production. *Nat. Commun.* **8**, 14650 (2017).
22. X. Zhang, M. Li, A. Agrawal, K. Y. San, Efficient free fatty acid production in *Escherichia coli* using plant acyl-ACP thioesterases. *Metab. Eng.* **13**, 713–722 (2011).
23. Z. Rahman *et al*., Enhanced production of fatty acid ethyl ester with engineered *fabHDG* operon in *Escherichia coli*. *Microorganisms* **7**, 552 (2019).
24. J. Wu, P. Zhou, X. Zhang, M. Dong, Efficient *de novo* synthesis of resveratrol by metabolically engineered *Escherichia coli*. *J. Ind. Microbiol. Biotechnol.* **44**, 1083–1095 (2017).
25. M. Klaus, A. D. D'Souza, A. Nivina, C. Khosla, M. Grininger, Engineering of chimeric polyketide synthases using SYNZIP docking domains. *ACS Chem. Biol.* **14**, 426–433 (2019).
26. E. Rossini, J. Gajewski, M. Klaus, G. Hummer, M. Grininger, Analysis and engineering of substrate shuttling by the acyl carrier protein (ACP) in fatty acid synthases (FASs). *Chem. Commun.* **54**, 11606–11609 (2018).
27. J. Gajewski *et al*., Engineering fatty acid synthases for directed polyketide production. *Nat. Chem. Biol.* **13**, 363–365 (2017).
28. S. Murli *et al*., Chemobiosynthesis of novel 6-deoxyerythronolide B analogues by mutation of the loading module of 6-deoxyerythronolide B synthase 1. *Appl. Environ. Microbiol.* **71**, 4503–4509 (2005).
29. M. C. Walker *et al*., Expanding the fluorine chemistry of living systems using engineered polyketide synthase pathways. *Science* **341**, 1089–1094 (2013).
30. B. J. Dunn, D. E. Cane, C. Khosla, Mechanism and specificity of an acyltransferase domain from a modular polyketide synthase. *Biochemistry* **52**, 1839–1841 (2013).
31. K. J. Weissman, Genetic engineering of modular PKSs: From combinatorial biosynthesis to synthetic biology. *Nat. Prod. Rep.* **33**, 203–230 (2016).
32. A. M. Marcella, A. W. Barb, A rapid fluorometric assay for the S-malonyltransacylase FabD and other sulfhydryl utilizing enzymes. *J. Biol. Methods* **3**, 1–10 (2016).
33. A. E. Szafranska, T. S. Hitchman, R. J. Cox, J. Crosby, T. J. Simpson, Kinetic and mechanistic analysis of the malonyl CoA:ACP transacylase from *Streptomyces coelicolor* indicates a single catalytically competent serine nucleophile at the active site. *Biochemistry* **41**, 1421–1427 (2002).
34. A. M. Marcella, A. W. Barb, Acyl-coenzyme A:(*holo*-acyl carrier protein) transacylase enzymes as templates for engineering. *Appl. Microbiol. Biotechnol.* **102**, 6333–6341 (2018).
35. A. M. Marcella, A. W. Barb, The R117A variant of the *Escherichia coli* transacylase FabD synthesizes novel acyl-(acyl carrier proteins). *Appl. Microbiol. Biotechnol.* **101**, 8431–8441 (2017).
36. A. T. Keatinge-Clay *et al*., Catalysis, specificity, and ACP docking site of *Streptomyces coelicolor* malonyl-CoA:ACP transacylase. *Structure* **11**, 147–154 (2003).
37. L. Zhang *et al*., Malonyl-CoA: Acyl carrier protein transacylase from *Helicobacter pylori*: Crystal structure and its interaction with acyl carrier protein. *Protein Sci.* **16**, 1184–1192 (2007).
38. A. Miyanaga, S. Iwasawa, Y. Shinohara, F. Kudo, T. Eguchi, Structure-based analysis of the molecular interactions between acyltransferase and acyl carrier protein in vicenistatin biosynthesis. *Proc. Natl. Acad. Sci. U.S.A.* **113**, 1802–1807 (2016).
39. A. Miyanaga *et al*., Structural basis of protein-protein interactions between a *trans*-acting acyltransferase and acyl carrier protein in polyketide disorazole biosynthesis. *J. Am. Chem. Soc.* **140**, 7970–7978 (2018).
40. A. M. Gulick, C. C. Aldrich, Trapping interactions between catalytic domains and carrier proteins of modular biosynthetic enzymes with chemical probes. *Nat. Prod. Rep.* **35**, 1156–1184 (2018).
41. K. Finzel, D. J. Lee, M. D. Burkart, Using modern tools to probe the structure-function relationship of fatty acid synthases. *ChemBioChem* **16**, 528–547 (2015).
42. J. T. Mindrebo *et al*., "Structural basis of acyl-carrier protein interactions in fatty acid and polyketide biosynthesis" in *Comprehensive Natural Products III: Chemistry and Biology*, Hung-wen Liu, Tadhg Begley, Eds. (Elsevier, 2019).
43. A. S. Worthington, M. D. Burkart, One-pot chemo-enzymatic synthesis of reporter-modified proteins. *Org. Biomol. Chem.* **4**, 44–46 (2006).
44. J. C. Milligan *et al*., Molecular basis for interactions between an acyl carrier protein and a ketosynthase. *Nat. Chem. Biol.* **15**, 669–671 (2019).
45. G. J. Dodge *et al*., Structural and dynamical rationale for fatty acid unsaturation in *Escherichia coli*. *Proc. Natl. Acad. Sci. U.S.A.* **116**, 6775–6783 (2019).
46. C. Nguyen *et al*., Trapping the dynamic acyl carrier protein in fatty acid biosynthesis. *Nature* **505**, 427–431 (2014).
47. J. T. Mindrebo *et al*., Gating mechanism of elongating β-ketoacyl-ACP synthases. *Nat. Commun.* **11**, 1727 (2020).
48. T. D. Davis, J. M. Michaud, M. D. Burkart, Active site labeling of fatty acid and polyketide acyl-carrier protein transacylases. *Org. Biomol. Chem.* **17**, 4720–4724 (2019).
49. F. T. Wong, X. Jin, I. I. Mathews, D. E. Cane, C. Khosla, Structure and mechanism of the *trans*-acting acyltransferase from the disorazole synthase. *Biochemistry* **50**, 6539–6548 (2011).
50. C. Oefner, H. Schulz, A. D'Arcy, G. E. Dale, Mapping the active site of *Escherichia coli* malonyl-CoA-acyl carrier protein transacylase (FabD) by protein crystallography. *Acta Crystallogr. D Biol. Crystallogr.* **62**, 613–618 (2006).
51. A. Rittner, K. S. Paithankar, K. V. Huu, M. Grininger, Characterization of the polyspecific transferase of murine type I fatty acid synthase (FAS) and implications for polyketide synthase (PKS) engineering. *ACS Chem. Biol.* **13**, 723–732 (2018).
52. A. Rittner, K. S. Paithankar, A. Himmler, M. Grininger, Type I fatty acid synthase trapped in the octanoyl-bound state. *Protein Sci.* **29**, 589–605 (2020).
53. G. Pappenberger *et al*., Structure of the human fatty acid synthase KS-MAT didomain as a framework for inhibitor design. *J. Mol. Biol.* **397**, 508–519 (2010).
54. F. Zhang *et al*., Structural insights into the substrate specificity of acyltransferases from salinomycin polyketide synthase. *Biochemistry* **58**, 2978–2986 (2019).
55. C. D. Reeves *et al*., Alteration of the substrate specificity of a modular polyketide synthase acyltransferase domain through site-specific mutations. *Biochemistry* **40**, 15464–15470 (2001).
56. J. E. Cronan, The chain-flipping mechanism of ACP (acyl carrier protein)-dependent enzymes appears universal. *Biochem. J.* **460**, 157–163 (2014).
57. F. Colizzi, M. Masetti, M. Recanatini, A. Cavalli, Atomic-level characterization of the chain-flipping mechanism in fatty-acids biosynthesis. *J. Phys. Chem. Lett.* **7**, 2899–2904 (2016).
58. J. R. Gallagher, S. T. Prigge, Plasmodium falciparum acyl carrier protein crystal structures in disulfide-linked and reduced states and their prevalence during blood stage growth. *Proteins* **78**, 575–588 (2010).
59. A. K. Sharma, S. K. Sharma, A. Surolia, N. Surolia, S. P. Sarma, Solution structures of conformationally equilibrium forms of *holo*-acyl carrier protein (PfACP) from *Plasmodium falciparum* provides insight into the mechanism of activation of ACPs. *Biochemistry* **45**, 6904–6916 (2006).
60. S. E. Evans *et al*., An ACP structural switch: Conformational differences between the *apo* and *holo* forms of the actinorhodin polyketide synthase acyl carrier protein. *ChemBioChem* **9**, 2424–2432 (2008).
61. D. I. Chan, T. Stockner, D. P. Tieleman, H. J. Vogel, Molecular dynamics simulations of the Apo-, Holo-, and acyl-forms of *Escherichia coli* acyl carrier protein. *J. Biol. Chem.* **283**, 33620–33629 (2008).
62. A. S. Worthington, D. F. Porter, M. D. Burkart, Mechanism-based crosslinking as a gauge for functional interaction of modular synthases. *Org. Biomol. Chem.* **8**, 1769–1772 (2010).
63. A. S. Worthington *et al*., Probing the compatibility of type II ketosynthase-carrier protein partners. *ChemBioChem* **9**, 2096–2103 (2008).
64. K. Finzel *et al*., Probing the substrate specificity and protein-protein interactions of the *E. coli* fatty acid dehydratase, FabA. *Chem. Biol.* **22**, 1453–1460 (2015).
65. J. F. Barajas *et al*., Structural and biochemical analysis of protein-protein interactions between the acyl-carrier protein and product template domain. *Angew. Chem. Int. Ed. Engl.* **55**, 13005–13009 (2016).
66. J. Molnos, R. Gardiner, G. E. Dale, R. Lange, A continuous coupled enzyme assay for bacterial malonyl-CoA:acyl carrier protein transacylase (FabD). *Anal. Biochem.* **319**, 171–176 (2003).
67. V. S. Rangan, S. Smith, Alteration of the substrate specificity of the malonyl-CoA/acetyl-CoA:acyl carrier protein S-acyltransferase domain of the multifunctional fatty acid synthase by mutation of a single arginine residue. *J. Biol. Chem.* **272**, 11975–11978 (1997).
68. M. Malinska, M. Dauter, Z. Dauter, Geometry of guanidinium groups in arginines. *Protein Sci.* **25**, 1753–1756 (2016).